

Simulation of the turbulent axisymmetric bluff body wake with pulsed jet forcing

Taihang Zhu * and Jonathan F. Morrison *Department of Aeronautics, Imperial College London, SW7 2AZ London, United Kingdom*

(Received 21 June 2021; accepted 1 November 2021; published 16 December 2021)

The turbulent axisymmetric bluff body wake is studied with a large eddy simulation (LES). The effect of pulsed jet forcing on the wake is investigated. For completeness, the pulsed jet actuator is included in the computational domain. Spectral proper orthogonal decomposition (SPOD) is applied to analyze the wake and the effect of pulsed jet forcing. The numerical results show good agreement with the experimental results and successfully reproduce the dominant modes of the axisymmetric wake. SPOD identifies the axisymmetric bubble pumping mode ($St_D = 0.06$), axisymmetric-breaking vortex shedding mode ($St_D = 0.22$), and an axisymmetric-breaking mode close to the subharmonic of the shedding mode ($St_D = 0.1$). When the high-frequency pulsed jet ($St_\theta = 0.107$) is applied to the wake, the pressure fluctuation on the base and the azimuthal modes are globally weakened without any mode selection. The mean flow properties show that the inlet flow is driven towards the wake centerline by the high-frequency jet, and the shear layer deviates, forming a concave separation streamline. The entrainment in the wake is suppressed, and the wake is narrowed, leading to a global pressure rise. The high-frequency pulsed jet is concentric and greatly enhances the entrainment in the vicinity of the separation point. A low-pressure region is generated there, which drives the inlet flow towards the wake. Low-frequency forcing ($St_\theta = 0.029$) generates a diffusive pulsed jet which enhances the mixing and entrainment in its trajectory. Low-frequency forcing reduces the wake length and accelerates recirculating flow near the base, leading to a reduction in base pressure, and the vortex shedding mode ($St_D = 0.2$) is amplified.

DOI: [10.1103/PhysRevFluids.6.124604](https://doi.org/10.1103/PhysRevFluids.6.124604)

I. INTRODUCTION

At high Reynolds number, the flow separation near the bluff body trailing edge forms a turbulent wake. The low pressure in the wake and high pressure on the bluff body nose creates pressure drag, which is the main source of bluff body aerodynamic drag. For economic and environmental reasons [1], the bluff body wake is one of the main topics in aerodynamic research [2–11] and turbulent flow control [12–21]. For the rectangular-sectioned bluff body, two dominant mechanisms are present [3]. The interactions between the shear layers near the opposite trailing edges cause weak oscillation at a relatively high frequency. The other more energetic dynamic is the bistability in which the recirculation zone shows random shifting between two preferred positions on a timescale which is $\mathcal{O}(1000)$ times the convective timescale [3]. Statistically, the three-dimensional (3D) wake with reflectional symmetry is only achieved over a long-time average. Unlike the bistability of the rectangular-sectioned bluff body wake, the axisymmetric bluff body wake is characterized by the random shifting of the vortex shedding plane over an infinite number of azimuthal states [2], leading to a multistable wake. The wake asymmetry behavior is also found

*taihang.zhu17@imperial.ac.uk

in the turbulent sphere wake [22]. The multistability is random in nature and the timescale of the shift is about $TU_\infty/D = 500$ ($St_D = 0.002$) [5]. In addition to the multistability, the premultiplied azimuthal spectra show that there are three more modes in the axisymmetric bluff body, including the vortex shedding mode ($St_D = 0.2$), the mode close to the subharmonic of the shedding mode ($St_D = 0.1$), and the bubble pumping mode ($St_D = 0.06$) [2]. Due to the complex dynamics and large timescale of the wake shifting, the turbulent bluff wake is a challenge for numerical simulation. Successful large eddy simulation (LES) of the bistable rectangular-sectioned bluff body wake was recently conducted by Dalla Longa *et al.* [9] and Fan *et al.* [23]. A successful LES of the turbulent axisymmetric bluff body wake, which exhibits more complicated multistability, is relatively rare.

To control the wake and recover the base pressure, one of the most successful strategies is to apply a pulsed jet (a “synthetic” jet, or “zero-net-mass-flux” jet) [24] in the vicinity of the separation point. Pastoor *et al.* [14] applied a pulsed jet with a forcing frequency lower than the vortex shedding frequency to a turbulent wake generated by a bluff body with rectangular cross section. A base pressure recovery of 40% is achieved, leading to 15% total aerodynamic drag reduction. This pulsed jet can synchronize the shear layer development and decouple the vortex formation. The dead water region is enlarged, leading to a base pressure recovery. The numerical study by Parkin *et al.* [17] and Krajnović and Fernandes [25] also show that the main effect of this kind of pulsed jet is to produce symmetric vortex shedding in the near wake and extend the mean recirculation bubble.

More recently, the experimental study by Morrison and Qubain [26] shows that the high-frequency pulsed jet (at least one order of magnitude higher than the vortex shedding frequency) applied to an axisymmetric bluff body wake achieved base pressure recovery. The mechanism of this base pressure recovery is different from that of Pastoor *et al.* [14] since the pulsed jet is in the high-frequency range. The axisymmetric bluff body wake is also different from the rectangular-sectioned bluff body wake characterized by strong global vortex shedding. Oxlade *et al.* [13] conducted a comprehensive experimental study showing that the pulsed jet can increase the base pressure in the rear of the bluff body by up to 33% at a forcing frequency of $St_\theta \approx 0.11$ ($St_D \approx 9.8$) and amplitude of $C_\mu = 0.04$. Cabitza [27] achieved a similar result with a rectangular-sectioned bluff body. At $St_H \approx 13.9$ and $C_\mu = 0.168$, the high-frequency pulsed jet can increase the base pressure by 27.7%, equivalent to a reduction of 13.1% in total drag. Similarly, Barros *et al.* [18] applied a pulsed jet with positive mass flux to the bluff body wake, and exploiting the Coanda effect also, achieved about 20% drag reduction. The present study found that without the Coanda effect, the effect of this positive-mass-flux pulsed jet to the wake is similar to the zero-net-mass-flux pulsed jet used by Oxlade *et al.* [13].

Even though the high-frequency pulsed jet has been successfully applied to control bluff body wake, the base pressure recovery mechanism is not fully understood. The study by Oxlade *et al.* [13] shows that the base pressure recovery is associated with the suppression of entrainment and a reduction in turbulence fluctuations. The azimuthal mode decomposition result shows that, instead of targeting a specific mode, the high-frequency pulsed jet causes a global weakening of all the modes. The study by Barros *et al.* [18] shows that the pulsed jet can deviate the separated shear layer without geometric modification and causes the fluidic boat-tailing effect. It shows that the deviation of the separated shear layer is caused by the vectoring effect of the pulsed jet [24], i.e., the primary flow can be deviated towards the pulsed jet when the high-frequency pulsed jet is applied near the edge. However, a detailed analysis of how the vectoring effect deviates the inlet flow is not fully understood. In agreement with the result by Oxlade *et al.* [13], a reduction in entrainment also appears in the study by Barros *et al.* [18]. The turbulence structures observed on the cross-plane two diameters downstream of the jet exit show that the axisymmetric mixing layer is dominated by streamwise vortices, which are related to $m = 0$ and $m = 1$ perturbations [28].

In the present study, the turbulent axisymmetric bluff body wake and the effect of pulsed jet forcing on the wake are investigated using LES, at a Reynolds number $\sim 2 \times 10^5$. A description and validation of the numerical scheme are provided in Sec. II. The results are provided in Sec. III. Section IV provides a summary of the main results.

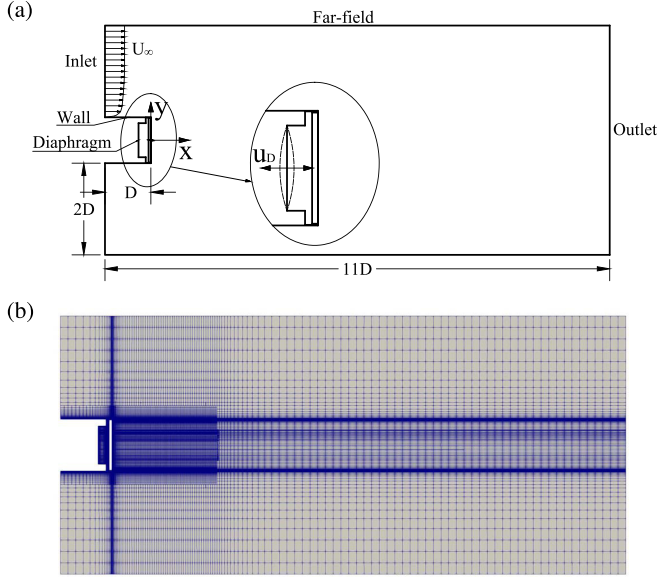


FIG. 1. Numerical setup. (a) The computational domain and (b) the mesh.

II. CONFIGURATIONS

A. Numerical scheme

As is shown in Fig. 1, the computational domain extends from the back section of the bluff body with diameter $D = 0.1965$ m to the far field. The diameter and the length of the whole domain are $5D$ and $11D$, respectively. The actuator diaphragm and the cavity are included in the computational domain to resolve the jet structure fully. A velocity boundary condition is prescribed on the diaphragm to compress and depress the cavity fluid to generate the pulsed jet. The diaphragm motion is described by

$$u_D(y, z, t) = (ay^2 + az^2 - \frac{1}{4}aD^2)2\pi f \cos(2\pi ft), \quad (1)$$

where a is a constant. This method has been validated by Zhu *et al.* [29]. The pressure coefficient C_p is defined as

$$C_p = \frac{p - p_\infty}{\frac{1}{2}\rho U_\infty^2}, \quad (2)$$

where p_∞ is the reference pressure. The area-weighted averaged pressure coefficient on the base surface is

$$\langle C_p \rangle = \frac{1}{A_b} \int_\phi \int_r C_p(r, \phi) r dr d\phi, \quad (3)$$

where A_b is the area of the base. Following Oxlade *et al.* [13], the area-weighted time-averaged mean pressure coefficient is denoted as $\overline{\langle C_p \rangle}$. The velocity coefficient is defined as

$$C_\mu = \frac{u_j^2 A_j}{U_\infty^2 A_b}, \quad (4)$$

where A_j is the area of the slot, u_j is the pulsed jet velocity at the axis of the slot. The natural mode frequency is expressed as Strouhal number $St_D = fU_\infty/D$. The forcing frequency is $St_\theta = fU_\infty/\theta$, where θ is the momentum thickness of the boundary layer, $\theta = 2.14$ mm.

TABLE I. Numerical settings and comparison with the experimental result by Oxlade *et al.* [13].

Case	f (Hz)	St_θ	C_μ	L/D		$\overline{\langle C_p \rangle}$	
				Numerical	Experimental	Numerical	Experimental
Unforced				1.28	1.27	-0.125	-0.121
Low-frequency forced (LF)	200	0.029	0.030	1.13		-0.14	-0.157
High-frequency forced (HF)	750	0.107	0.058	1.1		-0.1	-0.096

The open-source package OPENFOAM is used to perform a numerical study of the axisymmetric bluff-body wake. A large eddy simulation (LES) is performed with a one-equation eddy-viscosity subgrid-scale (SGS) model [30] where the turbulence kinetic energy is given by

$$\frac{D}{Dt}(\rho k) = \nabla \cdot (\rho D_k \nabla k) + \rho G - \frac{2}{3} \rho k \nabla \cdot \mathbf{u} - \frac{C_e \rho k^{1.5}}{\Delta} + S_k. \quad (5)$$

The three-dimensional compressible Navier-Stokes equation is solved based on the Pimple algorithm. The second-order discretization is used in the numerical scheme. Following the experimental study by Oxlade *et al.* [13], the free-stream velocity is 15 m/s on the inlet boundary. The Reynolds number based on the diameter of the base is $Re_D \sim 2 \times 10^5$. On the inlet boundary near the wall, the inlet velocity is prescribed according to the law of the wall:

$$\begin{cases} U = U_\infty, & y^+ > \delta^+, \\ U^+ = \frac{1}{\kappa} \ln y^+ + C^+, & \delta^+ \geq y^+ > y_i^+, \\ U^+ = y^+, & y^+ \leq y_i^+, \end{cases} \quad (6)$$

where y_i^+ is the intersection location of these two equations in the buffer layer, $y^+ = y U_\tau / \nu$, $U^+ = U / U_\tau$, $\delta^+ = \delta U_\tau / \nu$, δ is the thickness of the boundary layer, U_τ is the friction velocity, and $\kappa = 0.41$, $C^+ = 5$. A nonreflecting pressure boundary condition is used on the boundary of the computational domain. A no-slip boundary condition is applied on the wall of the actuator and the bluff body. A total nondimensional timescale of $TU_\infty/D = 5500$ is resolved, covering 1200 vortex shedding periods, 320 bubble pumping periods, and about 10 random multistability wake shifts. A hexahedral mesh with a total number of 4.5 million nodes is used with refinement near the wake. In the near-wall region, the mesh size is refined to keep the maximum $y_{\max}^+ < 5$. An adjustable time interval is used to keep the Courant number less than 0.7. A total of 2.5×10^4 sampling points is uniformly distributed on the base to achieve time- and space-resolved data to perform SPOD. A detailed description of the meshing scheme and the numerical scheme can be found in Zhu *et al.* [29].

B. Validation

Table I shows the three cases in the current study, including the unforced bluff body wake, the low-frequency forced wake, and the high-frequency forced wake [13]. The low-frequency forcing frequency is still much higher than that studied by Pastoor *et al.* [14] and Parkin *et al.* [17]. It is clear that, in the unforced case, both the rear stagnation point location L and the mean base pressure coefficient $\overline{\langle C_p \rangle}$ agree well with the experimental result. In the forced cases, $\overline{\langle C_p \rangle}$ is also close to the experimental value.

The instantaneous flow field (Fig. 2) is identified by the Q criterion. In the unforced case, the sharp trailing edge causes flow separation and forms a turbulent wake. Downstream, these turbulence structures develop into some quasistreamwise braids which resemble the streamwise vortices in the turbulent mixing layer observed by Davoust *et al.* [28]. The mean flow field shows

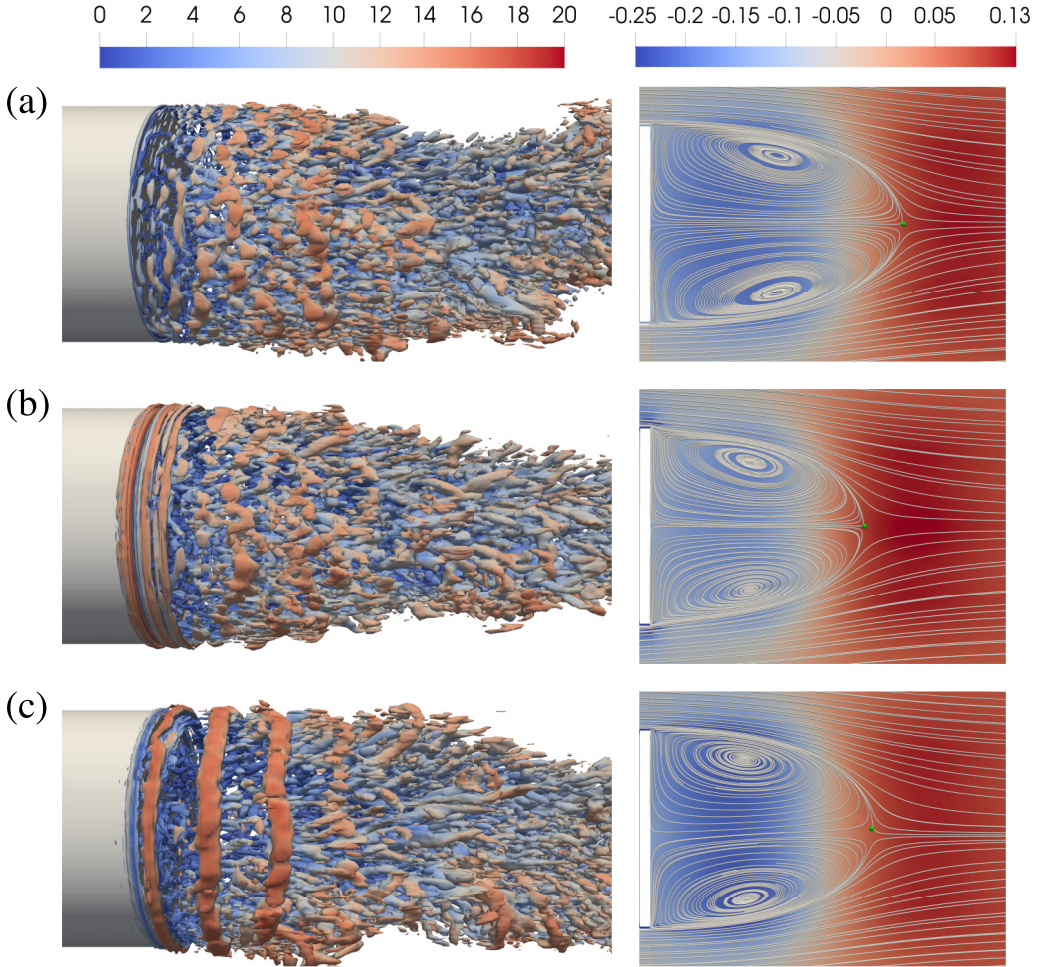


FIG. 2. The instantaneous flow field identified by the Q criterion (colored by the velocity magnitude, $0 < \overline{U} < 20 \text{ ms}^{-1}$) and the time-averaged streamline and pressure field ($-0.25 < \overline{C_p} < 0.13$) for (a) the unforced wake, (b) the high-frequency forced wake, and (c) the low frequency forced wake. The green dot shows the location of the stagnation point.

that a reflectional-symmetric mean velocity streamline is achieved. The pressure field shows that low mean pressure is generated near the vortex core and in the shear layer. In the high-frequency (HF) forced case, some concentric vortex rings are generated in the vicinity of the base edge. The wake width is reduced compared to the unforced case. The mean pressure in the wake is also higher than in the unforced case. In the low-frequency (LF) case, vortex rings are generated by the pulsed jet and propagate further downstream. Some quasistreamwise braids are generated downstream. In the mean pressure field, the pressure in the wake is lower than that in the unforced case, especially in the vortex core and shear layer.

Following Rigas *et al.* [2], azimuthal mode decomposition is performed with the pressure data at eight azimuthal locations. The pre-multiplied azimuthal frequency spectra showing the azimuthal spectral energy Φ_m distributed over St_D are illustrated in Fig. 3. The spectra are pre-multiplied so that the area under the curve represents the mean-square pressure. There are three peaks in this figure, which are summarized in Table II. The first peak *a* corresponds to the bubble pumping mode. It peaks at $St_D = 0.06$, which is the same as the experimental value. The second peak *b* is close to

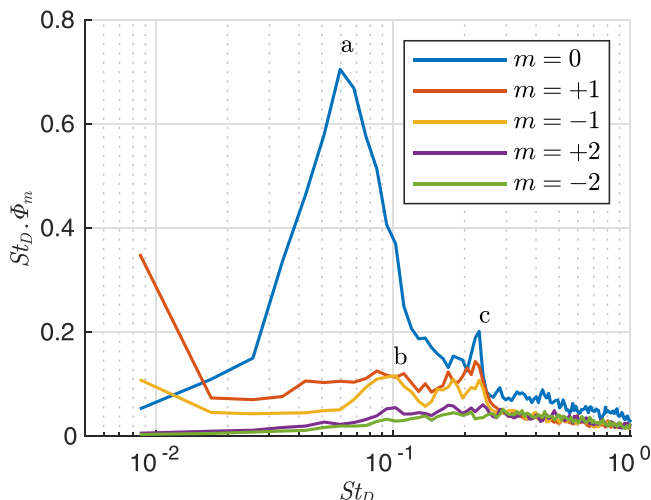


FIG. 3. Premultiplied pressure spectra for azimuthal modes of the unforced wake. *a* indicates the bubble pumping mode ($St_D = 0.06$), *b* the mode close to the subharmonic of the shedding mode ($St_D = 0.1$), and *c* the vortex shedding mode ($St_D = 0.22$).

the subharmonic of the shedding mode. It locates at $St_D = 0.1$ in the numerical result, which is also the same as the experimental result. The third peak *c* is the vortex shedding mode. In the numerical result it is located at $St_D = 0.22$ which is close to the experimental value $St_D = 0.2$. The very-low-frequency (VLF) behavior, which exhibits multi-stable wake shift at a long timescale of about $TU_\infty/D = 500$ ($St_D = 0.002$), is not apparent in these spectra because the simulation extends over about ten VLF timescales, which is insufficient for averaging. However, the increase at low frequency ($St_D < 0.01$) for both modes $m = \pm 1$ is indicative of the VLF dynamics.

Figure 4 shows a comparison between the numerical velocity field in the wake and the experimental result. The numerical mean flow field shows excellent agreement with the experimental result, which shows that the mean velocity field is well resolved in the numerical work.

III. RESULTS

A. Dynamics of the unforced turbulent axisymmetric bluff body wake

The center of pressure (CoP) is calculated following Rigas *et al.* [5]. The nondimensional CoP in the Cartesian coordinate system is calculated by

$$\text{CoP}_x = \frac{1}{D \int p(t) dA} \int_A p(t) x dA, \quad \text{CoP}_y = \frac{1}{D \int p(t) dA} \int_A p(t) y dA, \quad (7)$$

where A is the area of the base. The CoP is then transformed into a polar coordinate system with radial position r and azimuthal position θ . The probability density function (PDF) of the CoP is

TABLE II. A comparison of the Strouhal number (St_D) of azimuthal modes between the numerical result and the experimental result by Rigas *et al.* [2]. The labels *a*, *b*, and *c* are shown in Fig. 3.

Label in Fig. 3	<i>a</i>	<i>b</i>	<i>c</i>
Numerical	0.06	0.1	0.2
Experimental	0.06	0.1	0.2

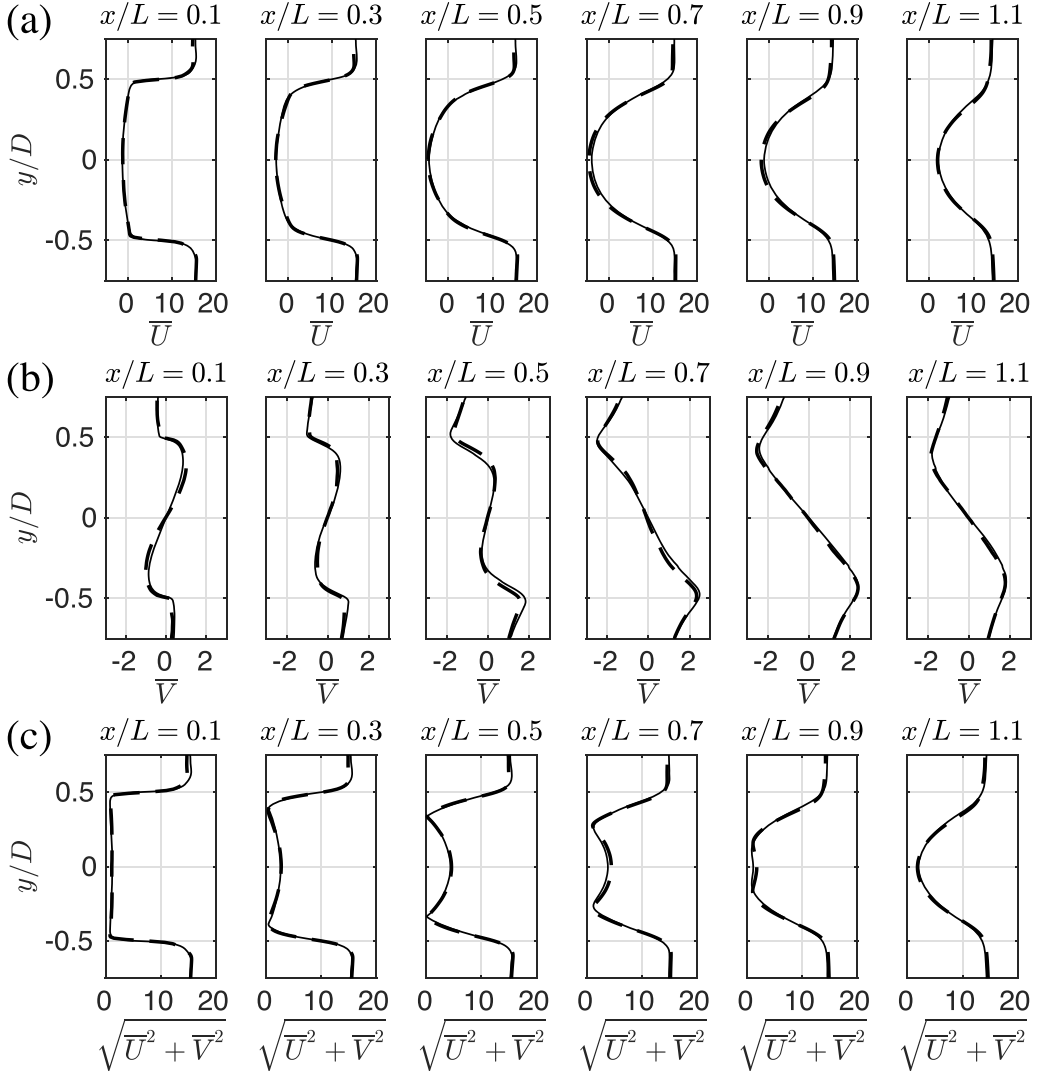


FIG. 4. Comparison of the mean velocity field between the numerical result (the solid line) and the experimental result (the dashed line). (a) The x component of the mean velocity \bar{U} . (b) The y component of the mean velocity \bar{V} . (c) The 2D mean velocity magnitude $\sqrt{\bar{U}^2 + \bar{V}^2}$.

shown in Fig. 5. It shows that the radial position of the CoP [Fig. 5(a)] is a nonzero fluctuating positive number, which indicates that the instantaneous wake is not axisymmetric in most cases. The radial position tends to lock near $r/D = 0.045$, which is larger than the experimental result ($r/D = 0.03$) by Rigas *et al.* [2]. Since the timescale of the very-low-frequency (VLF) wake shift is of the order $TU_\infty/D = 500$ and the wake shift is random at all the azimuthal positions, and due to insufficient averaging, the time-averaged wake is not perfectly axisymmetric, and the CoP is shifted slightly away from the center. The azimuthal position of the CoP [Fig. 5(b)] illustrates the multistable nature of the wake. It shows that, unlike the radial position, which is concentric near $r/D = 0.045$, the azimuthal position of the CoP can switch to any azimuthal angle. The probability of the azimuthal position is similar at some angles, which indicates that the wake is quasistabilized at these positions before randomly walking to another. In previous work by Dalla Longa *et al.*

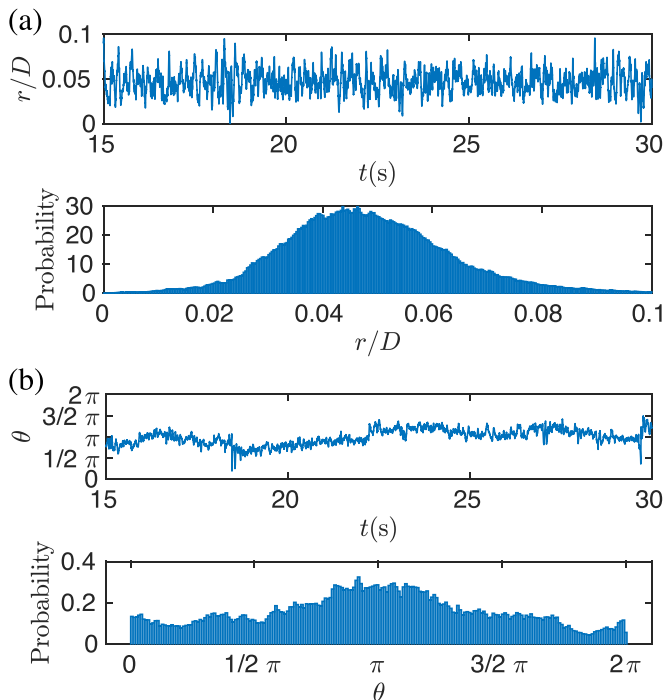


FIG. 5. A time series and PDF of the center of pressure for the unforced wake for (a) the radial position and (b) the azimuthal position.

[9] and Fan *et al.* [23], only one or two VLF wake shifts are simulated. With longer simulations, $TU_\infty/D = \mathcal{O}(100\,000)$, it is likely that the probability at all the azimuthal positions will be uniform.

Spectral proper orthogonal decomposition (SPOD) is performed based on the time-resolved base pressure data collected on a uniform Cartesian grid on the body base with 2.5×10^4 nodes. Compared with the space-only proper orthogonal decomposition (POD), SPOD is able to extract coherent structures oscillating at single frequency [31], which enables analysis into the dominant modes of the wake. Since the SPOD spectra are averaged over several overlapping blocks, SPOD is ideal for analyzing statistically stationary turbulent wake. This study decomposes the pressure data matrix P into data matrices P_f with a discrete Fourier transform (DFT). The cross-spectral density tensor at frequency f is written as

$$S_f = P_f P_f^H \quad (8)$$

and the SPOD eigenvalue problem is solved by

$$S_f W \Psi_f = \Psi_f \Lambda_f. \quad (9)$$

The SPOD modes are represented by the columns of Ψ_f and are ranked by the eigenvalues λ given by the diagonal matrix Λ_f .

As is shown in the premultiplied SPOD spectra in Fig. 6, three peaks can be identified at $St_D = 0.06$, $St_D = 0.1$, and $St_D = 0.22$. These peaks are very close to the experimental result by Rigas *et al.* [2]. The bubble pumping mode ($m = 0$, $St_D = 0.06$), an axisymmetric mode, represents the bulk of the energy in the spectrum. Both the vortex shedding ($St_D = 0.22$), and the mode close to its subharmonic ($St_D = 0.1$) are axisymmetric-breaking modes, for which reflectional symmetry is retained. Although the VLF dynamics are not apparent in the spectra, the dramatic rise near the low frequency, $St_D \approx 0.01$, is indicative of such a mode.

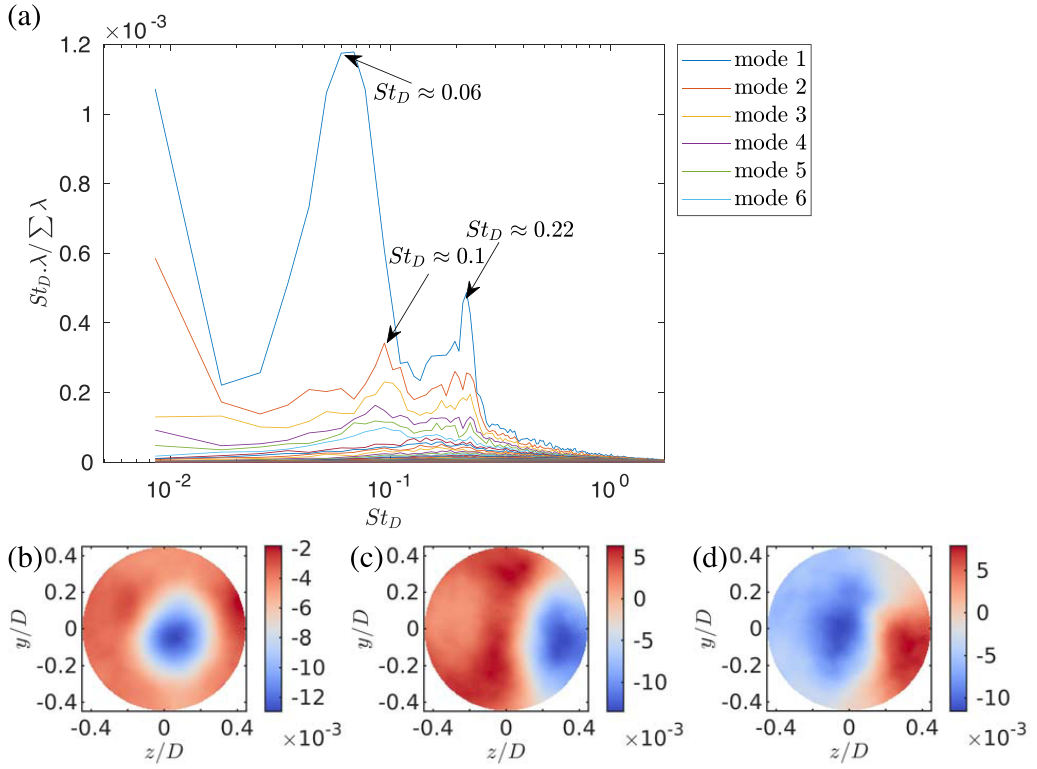


FIG. 6. Premultiplied SPOD spectra and SPOD modes based on the base pressure. (a) Premultiplied SPOD spectra, (b) the first mode at $St_D = 0.06$, (c) the second mode at $St_D = 0.1$, (d) the first mode at $St_D = 0.2$. Only the first six most energetic modes are labeled.

B. Global properties in the forced wake

The premultiplied frequency spectra per mode for the forced wake are shown in Fig. 7. They show peaks at the forcing frequency and higher harmonics. By comparing the HF and LF spectra

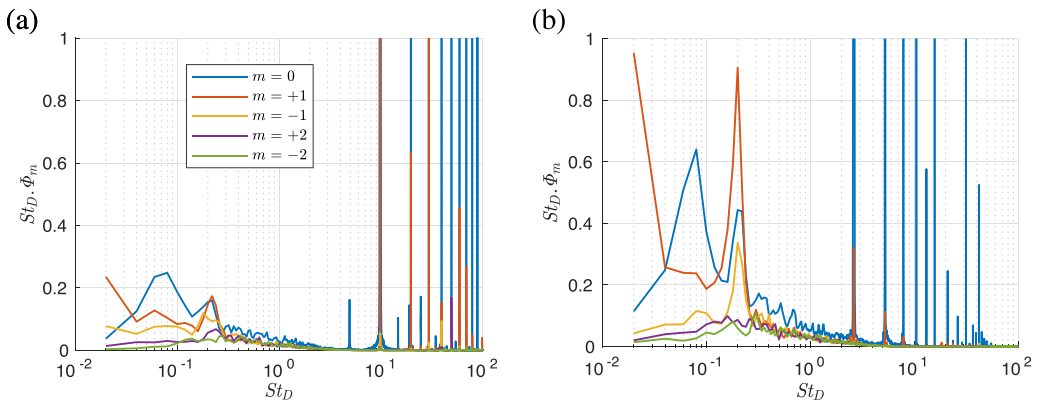


FIG. 7. Premultiplied azimuthal spectra for (a) the high-frequency forced wake and (b) the low-frequency forced wake. For comparison with the unforced spectra (Fig. 3), the peaks near $St_D = 0.06$ and $St_D = 0.2$ are labeled in the figure.

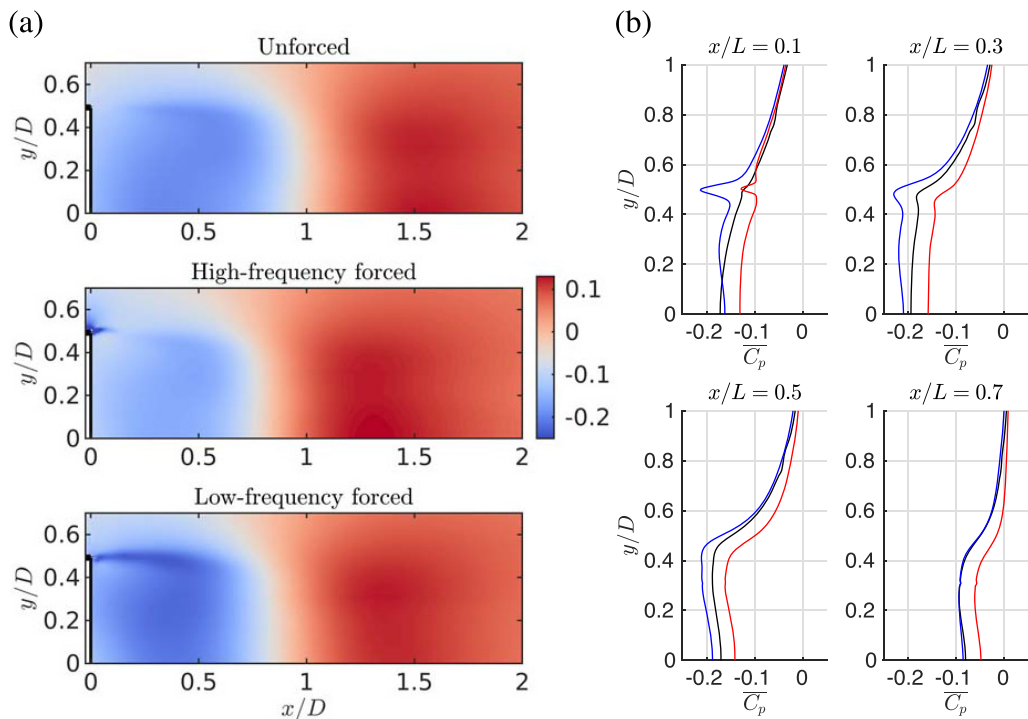


FIG. 8. (a) Distribution and (b) a comparison of the time-averaged pressure for the unforced wake (black), the high-frequency forced wake (red), and the low-frequency forced wake (blue).

with the unforced spectra (Fig. 3), it is clear that when the high-frequency pulsed jet is applied to the wake the azimuthal modes are globally weakened. It indicates that the high-frequency forcing can reduce the wake turbulence fluctuation, which agrees with the experimental result by Oxlade *et al.* [13]. The result also shows that the low-frequency pulsed jet can weaken the bubble pumping mode ($St_D = 0.06$), while the vortex shedding mode ($St_D = 0.2$) is amplified.

The mean pressure distribution in the wake is visualized in Fig. 8. In the unforced case, it shows that there is a low-pressure region in the shear layer and the recirculation area. The high-frequency forcing causes the pressure to rise in the whole wake and yet moves the wake closer to the base. There is a sharp pressure drop near the separation point, which is caused by the high entrainment in the local area. Similarly, the experimental result by Oxlade *et al.* [13] also found that in the trajectory of the pulsed jet there is a very-low pressure region. The low-frequency forcing causes a global pressure drop in the whole wake, especially in the trajectory of the pulsed jet.

The turbulence kinetic energy, $k = \frac{1}{2}(\overline{u^2} + \overline{v^2} + \overline{w^2})$ is shown in Fig. 9. In agreement with the result by Oxlade *et al.* [13] and Barros *et al.* [18], the high-frequency pulsed jet globally reduces turbulence kinetic energy in the wake (except near the separation point), thus reducing the entrainment in the wake. In the near wake ($x/L = 0.1$) the low-frequency jet reduces turbulence kinetic energy, whereas in the far wake ($x/L \geq 0.3$) the low-frequency pulsed jet increases the turbulence kinetic energy and the entrainment.

The Reynolds shear stress $-\overline{uv}$ normalized by $\overline{q^2}$ ($\overline{q^2} = 2k = \overline{u^2} + \overline{v^2} + \overline{w^2}$) is shown in Fig. 10(a). a_1 ($a_1 = -\overline{uv}/\overline{q^2}$) represents an efficiency of momentum flux and is relatively constant in a simple shear layer remote from an impermeable surface. In the forced cases, it shows an alternating sequence generated by vortices produced from the pulsed jet (Fig. 2). For the HF case the vortex structures are smaller and a_1 is dominated by negative values.

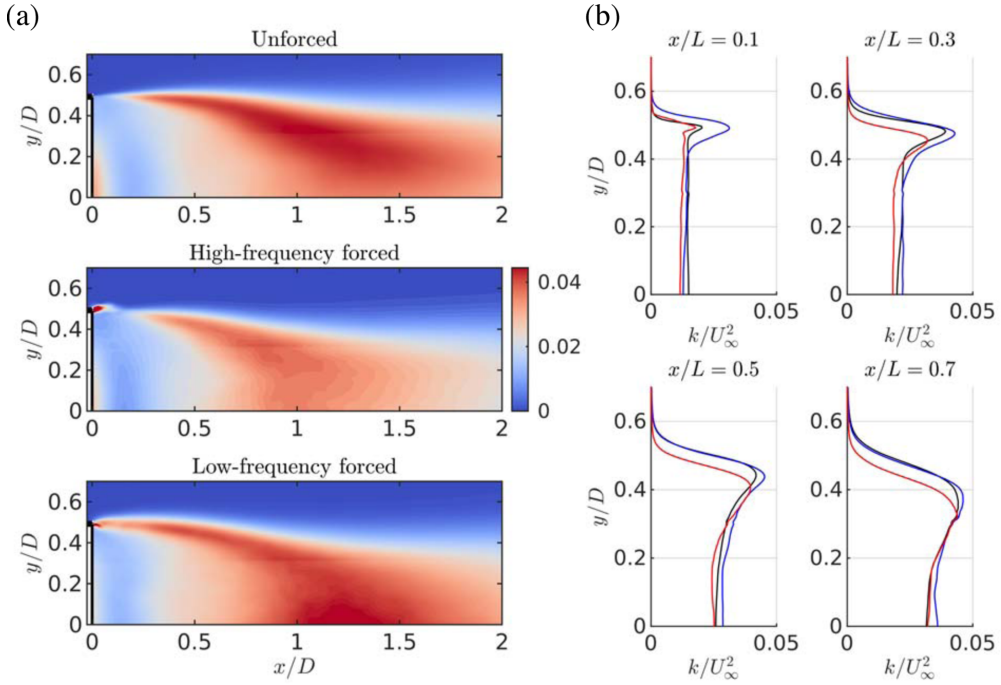


FIG. 9. (a) Distribution and (b) a comparison of the turbulence kinetic energy for the unforced wake (black), the high-frequency forced wake (red), and the low-frequency forced wake (blue).

C. Local properties near the separation point of the forced wake

The separation streamline marks the boundary between the wake and the inlet flow; see Fig. 11. Figure 11(b) shows that the high-frequency forcing effectively reshapes the separation streamline near the separation point. The angle of the separation streamline is significantly reduced, and the shear layer deviates toward the wake, forming a concave separation streamline. The width of the wake is narrowed, in agreement with the experimental observation by Oxlade *et al.* [13] and Barros *et al.* [18]. Although the low-frequency forcing reduces the wake length, its effect on the shape of the separation streamline is not as significant. Both the low-frequency forced wake and the unforced wake show a convex separation streamline near the separation point.

The shear-layer deviation can be attributed to the vectoring effect of the high-frequency pulsed jet [24]. As is shown in Fig. 12, the high-frequency pulsed jet effectively directs the flow near the separation point toward the wake [Fig. 12(a)]. Near the separation point, the high-frequency jet significantly increases the turbulence kinetic energy and enhances the local entrainment [Fig. 12(b)]. A very-low-pressure region is generated in this region [Fig. 12(c)], consistent with the vectoring effect described by Smith and Glezer [24]. The low-frequency pulsed jet effectively accelerates the flow motion near the base [Fig. 12(a)]. Whereas, it cannot drive the inlet flow toward the wake [Fig. 12(a)], and there is no very low pressure region in the vicinity of the separation point [Fig. 12(c)]. As a result, the vectoring effect is not evident in the low-frequency forced flow.

The vorticity field ω_z of the forced wake is collected on the z -normal cutting plane with 400×200 collecting points in the x and y directions. SPOD is performed based on these data; see Fig. 13. The SPOD spectra show a peak at the forcing frequency. The energy rank of the modes at the selected frequency ($St_\theta = 0.029$ for the low-frequency forcing and $St_\theta = 0.107$ for the high-frequency forcing) also shows low-rank behavior, i.e., energy is concentrated in the first mode. The first mode at the forcing frequency shows that the low-frequency pulsed jet is diffusive

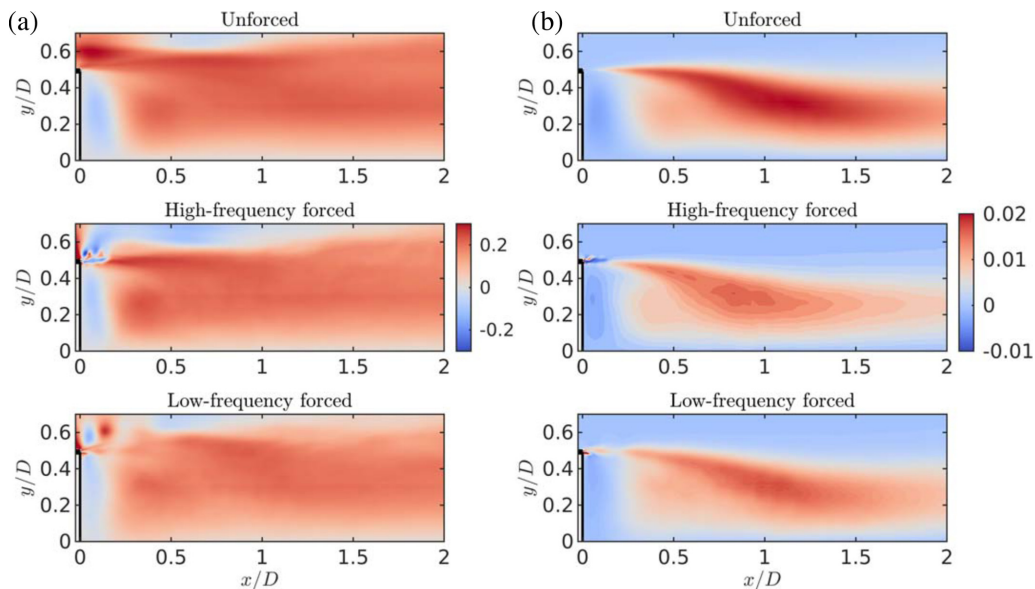


FIG. 10. The Reynolds shear stress $-\overline{uv}$ normalized by (a) $\overline{q^2}$ and (b) U_∞^2 .

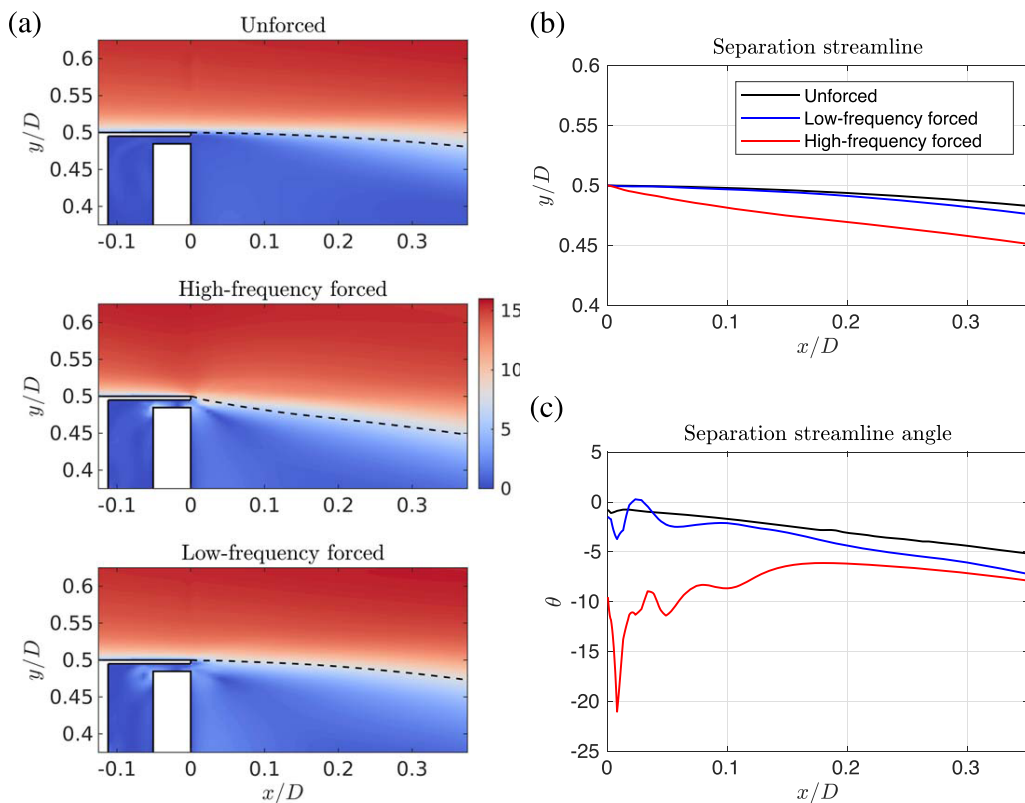


FIG. 11. (a) The time-averaged velocity magnitude and a comparison of (b) the separation streamline and (c) the streamline angle for the unforced wake (black), the high-frequency forced wake (red), and the low-frequency forced wake (blue). The dashed line shows the trajectory of the separation streamline.

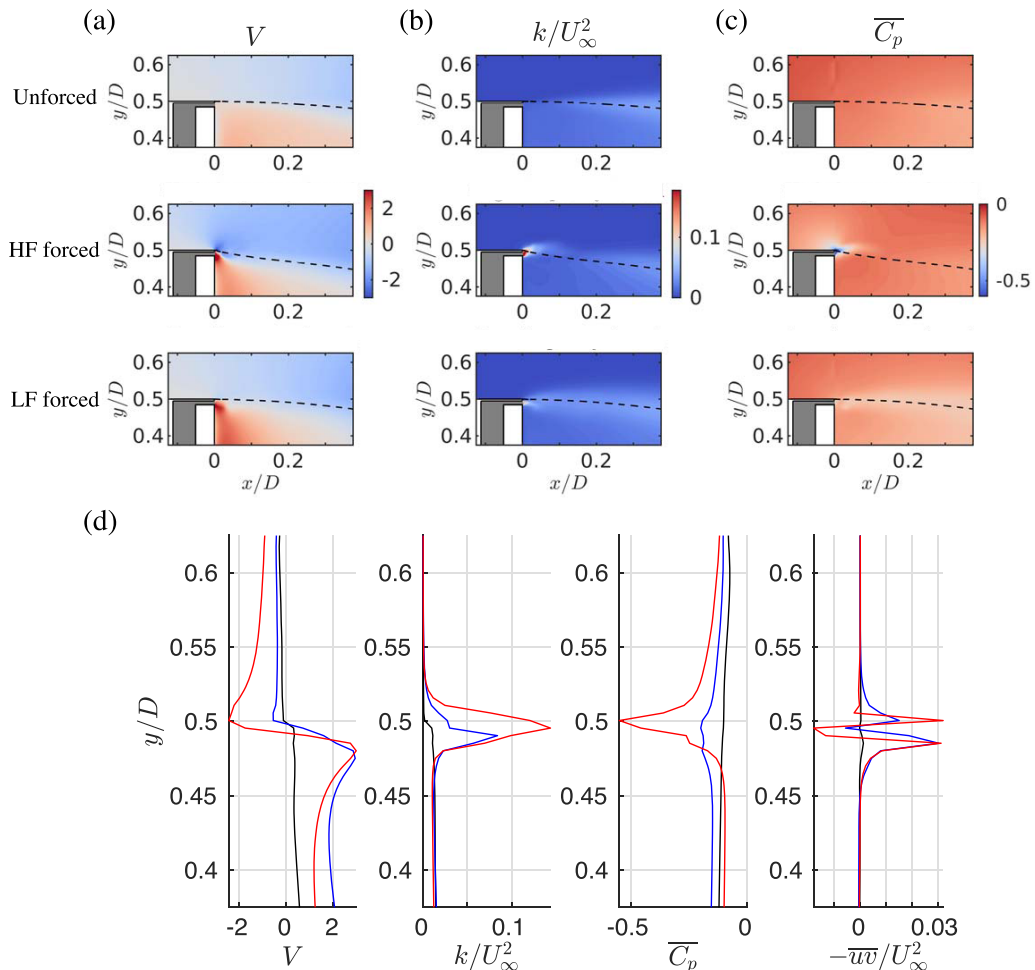


FIG. 12. (a) The y component of the time-averaged velocity V , (b) the turbulent kinetic energy k , and (c) the time-averaged pressure $\overline{C_p}$ in the vicinity of the separation point. (d) A comparison of the local properties, at $x/D = 0.01$, for the unforced wake (black), the high-frequency forced wake (red), and the low-frequency forced wake (blue). The dashed line shows the trajectory of the separation streamline.

and propagates further downstream. The pulsed jet enhanced the mixing along its trajectory, thus enhancing entrainment. The high-frequency pulsed jet is more concentric and rapidly decays moving downstream. Therefore, the entrainment is only enhanced in the vicinity of the separation point, which deviates the direction of the inlet flow toward the wake. As the pulsed jet rapidly disappears and the wake is narrowed downstream, the entrainment in the wake is globally suppressed.

IV. CONCLUSION

An LES of the turbulent axisymmetric bluff body wake is performed with and without the presence of pulsed jet forcing. The effect of the low-frequency forcing ($St_\theta = 0.029$) and high-frequency forcing ($St_\theta = 0.107$) on the bluff body wake is investigated. SPOD is performed to study the unforced bluff body wake and the structure of the pulsed jet.

The numerical result is validated against the experimental one of Rigas *et al.* [2] and Oxlade *et al.* [13]. Both the mean velocity field and the azimuthal spectra modes show excellent agreement

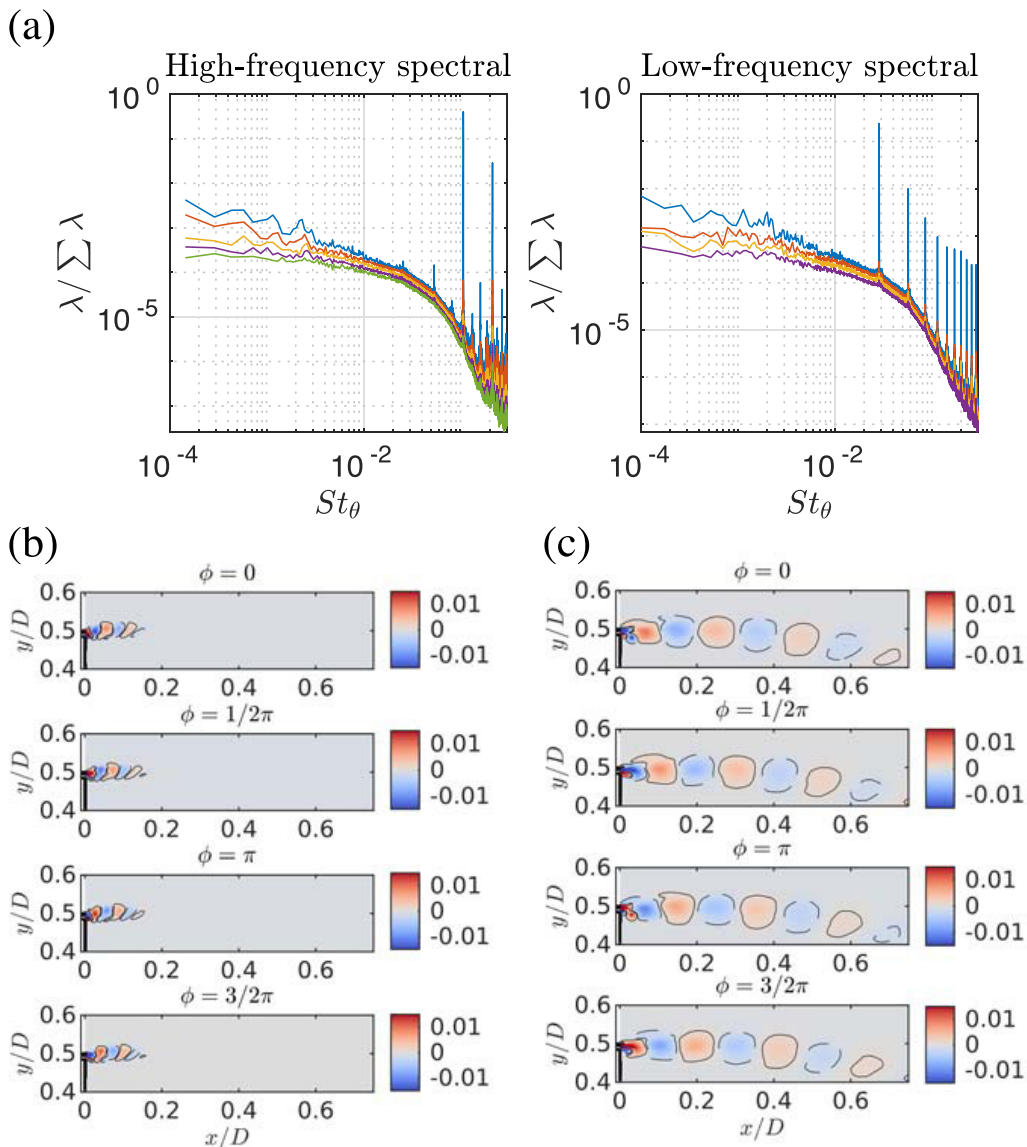


FIG. 13. (a) SPOD spectra of the forced wake and the SPOD modes at four different phases for (b) $St_\theta = 0.107$ and $St_\theta = 0.029$.

with the experimental result. The mean base pressure coefficient of the unforced flow and the forced flow also agrees well with the experimental result. The SPOD of the unforced flow also shows good agreement with the experimental result by Rigas *et al.* [2]. It shows that there is an axisymmetric bubble pumping mode ($St_D = 0.06$), an axisymmetric-breaking vortex shedding mode ($St_D = 0.22$), and an axisymmetric-breaking mode close to its subharmonic ($St_D = 0.1$). Reflectional symmetry is retained in these axisymmetric-breaking modes. The multistability of the axisymmetric wake is identified by inspecting the PDF of the CoP. By including the actuator in the computational domain, the 3D pulsed jet structures are resolved fully, providing high-fidelity numerical results and visualizing the effect of pulsed jet forcing. In addition, the viscous loss inside the actuator could be studied to find the energy loss caused by viscosity and improve the actuator

efficiency. For instance, the energy loss caused by pulsed jet flow separation through the actuator slot could be studied to improve the actuator design, and the boundary conditions for pulsed jet simulation can be studied [29].

The numerical result shows that the high-frequency pulsed jet can reduce pressure fluctuation and globally weaken all the azimuthal modes. The high-frequency jet is concentric and disappears rapidly downstream. When the high-frequency pulsed jet is applied to the wake, the entrainment in the wake is suppressed, the shear-layer deviates toward the wake and forms a concave separation streamline, and the wake is narrowed, leading to a global pressure rise in the wake. The deviation in the shear layer is caused by the vectoring effect of the high-frequency pulsed jet. In the vicinity of the separation point, the entrainment is greatly enhanced by the pulsed jet, resulting in a very low-pressure region, and drives the inlet flow toward the wake. As a result, the separation streamline deviates toward the wake centerline, leading to a narrower wake.

The low-frequency forcing generates a diffusive pulsed jet which propagates further downstream. It enhances the mixing and entrainment in its trajectory, reduces the wake length, and accelerates the recirculating flow near the base, leading to a pressure drop in the whole wake. Although it can reduce the length of the wake, its effect on the wake shape in the vicinity of the base is not as evident as the high-frequency forcing due to its limited ability to drive the inlet flow toward the wake. The azimuthal mode spectra show that when the low-frequency pulsed jet is applied, the bubble pumping mode ($St_D = 0.06$) is weakened while the vortex shedding mode ($St_D = 0.2$) is amplified.

-
- [1] N. Stern, The economics of climate change, *Am. Econ. Rev.* **98**, 1 (2008).
 - [2] G. Rigas, A. R. Oxlade, A. S. Morgans, and J. F. Morrison, Low-dimensional dynamics of a turbulent axisymmetric wake, *J. Fluid Mech.* **755**, R5 (2014).
 - [3] M. Grandemange, M. Gohlke, and O. Cadot, Turbulent wake past a three-dimensional blunt body. Part 1. Global modes and bi-stability, *J. Fluid Mech.* **722**, 51 (2013).
 - [4] M. Grandemange, M. Gohlke, and O. Cadot, Turbulent wake past a three-dimensional blunt body. Part 2. Experimental sensitivity analysis, *J. Fluid Mech.* **752**, 439 (2014).
 - [5] G. Rigas, A. S. Morgans, R. D. Brackston, and J. F. Morrison, Diffusive dynamics and stochastic models of turbulent axisymmetric wakes, *J. Fluid Mech.* **778**, R2 (2015).
 - [6] P. Bohorquez, E. Sanmiguel-Rojas, A. Sevilla, J. Jiménez-González, and C. Martínez-Bazán, Stability and dynamics of the laminar wake past a slender blunt-based axisymmetric body, *J. Fluid Mech.* **676**, 110 (2011).
 - [7] V. Gentile, F. Schrijer, B. Van Oudheusden, and F. Scarano, Low-frequency behavior of the turbulent axisymmetric near-wake, *Phys. Fluids* **28**, 065102 (2016).
 - [8] O. Evstafyeva, A. S. Morgans, and L. Dalla Longa, Simulation and feedback control of the Ahmed body flow exhibiting symmetry breaking behaviour, *J. Fluid Mech.* **817**, R2 (2017).
 - [9] L. Dalla Longa, O. Evstafyeva, and A. S. Morgans, Simulations of the bi-modal wake past three-dimensional blunt bluff bodies, *J. Fluid Mech.* **866**, 791 (2019).
 - [10] J. Ortiz-Tarin, S. Nidhan, and S. Sarkar, High-Reynolds-number wake of a slender body, *J. Fluid Mech.* **918**, A30 (2021).
 - [11] G. Pavia, M. Varney, M. Passmore, and M. Almond, Three dimensional structure of the unsteady wake of an axisymmetric body, *Phys. Fluids* **31**, 025113 (2019).
 - [12] S. L. Brunton and B. R. Noack, Closed-loop turbulence control: Progress and challenges, *Appl. Mech. Rev.* **67**, 050801 (2015).
 - [13] A. R. Oxlade, J. F. Morrison, A. Qubain, and G. Rigas, High-frequency forcing of a turbulent axisymmetric wake, *J. Fluid Mech.* **770**, 305 (2015).
 - [14] M. Pastoor, L. Henning, B. R. Noack, R. King, and G. Tadmor, Feedback shear layer control for bluff body drag reduction, *J. Fluid Mech.* **608**, 161 (2008).

-
- [15] J. Weller, S. Camarri, and A. Iollo, Feedback control by low-order modelling of the laminar flow past a bluff body, *J. Fluid Mech.* **634**, 405 (2009).
- [16] J. A. Dahan, A. S. Morgans, and S. Lardeau, Feedback control for form-drag reduction on a bluff body with a blunt trailing edge, *J. Fluid Mech.* **704**, 360 (2012).
- [17] D. J. Parkin, M. C. Thompson, and J. Sheridan, Numerical analysis of bluff body wakes under periodic open-loop control, *J. Fluid Mech.* **739**, 94 (2014).
- [18] D. Barros, J. Borée, B. R. Noack, A. Spohn, and T. Ruiz, Bluff body drag manipulation using pulsed jets and Coanda effect, *J. Fluid Mech.* **805**, 422 (2016).
- [19] R. D. Brackston, J. G. De La Cruz, A. Wynn, G. Rigas, and J. Morrison, Stochastic modelling and feedback control of bistability in a turbulent bluff body wake, *J. Fluid Mech.* **802**, 726 (2016).
- [20] G. Rigas, A. S. Morgans, and J. F. Morrison, Weakly nonlinear modelling of a forced turbulent axisymmetric wake, *J. Fluid Mech.* **814**, 570 (2017).
- [21] J. M. Garcia de la Cruz, A. R. Oxlade, and J. F. Morrison, Passive control of base pressure on an axisymmetric blunt body using a perimetric slit, *Phys. Rev. Fluids* **2**, 043905 (2017).
- [22] M. Grandemange, M. Gohlke, and O. Cadot, Statistical axisymmetry of the turbulent sphere wake, *Exp. Fluids* **55**, 1838 (2014).
- [23] Y. Fan, C. Xia, S. Chu, Z. Yang, and O. Cadot, Experimental and numerical analysis of the bi-stable turbulent wake of a rectangular flat-backed bluff body, *Phys. Fluids* **32**, 105111 (2020).
- [24] B. L. Smith and A. Glezer, Jet vectoring using synthetic jets, *J. Fluid Mech.* **458**, 1 (2002).
- [25] S. Krajnović and J. Fernandes, Numerical simulation of the flow around a simplified vehicle model with active flow control, *Int. J. Heat Fluid Flow* **32**, 192 (2011).
- [26] J. F. Morrison and A. Qubain, Control of an axisymmetric turbulent wake by a pulsed jet, in *Advances in Turbulence XII* (Springer, Berlin, 2009), pp. 225–228.
- [27] S. Cabitza, Active control of the wake from a rectangular-sectioned body, Ph.D. thesis, Imperial College London, 2014.
- [28] S. Davoust, L. Jacquin, and B. Leclaire, Dynamics of $m = 0$ and $m = 1$ modes and of streamwise vortices in a turbulent axisymmetric mixing layer, *J. Fluid Mech.* **709**, 408 (2012).
- [29] T. Zhu, Y. Pan, and J. F. Morrison, Numerical simulation on the pressure characteristics of the pulsed jet actuator (unpublished).
- [30] A. Yoshizawa, Statistical theory for compressible turbulent shear flows, with the application to subgrid modeling, *Phys. Fluids* **29**, 2152 (1986).
- [31] A. Towne, O. T. Schmidt, and T. Colonius, Spectral proper orthogonal decomposition and its relationship to dynamic mode decomposition and resolvent analysis, *J. Fluid Mech.* **847**, 821 (2018).